Through-process modelling of welding and service of 9Cr steel power plant components under load-following conditions

Padraig Mac Ardghail[1,2*], *Noel Harrison*[1,2], and *Sean B Leen*[1,2]

[1]Mechanical Engineering, College of Engineering and Informatics, NUI Galway, University Road, Galway, Ireland, H91 HX31.

[2]Ryan Institute for Environmental, Marine and Energy Research, NUI Galway, University Road, Galway, Ireland, H91 HX31.

Abstract. This paper is concerned with the development of a through-process model to predict the in-service performance of high-temperature, 9Cr steel, power plant components. A multi-pass welding simulation is conducted using the finite element software Abaqus. A user-material subroutine, including microstructure evolution and a physically-based constitutive model, is employed to predict the mechanical response of the material during welding and to predict welding residual stresses. Points are sampled from the FE geometry and their microstructure parameters and residual stress values are used in a uniaxial code to predict the relative in-service lives of the different weld regions under load-following power plant operating conditions. It is shown that post-weld heat treatment significantly improves predicted life and that there is a strong correlation between predicted microstructure before service and the predicted in-service life.

1 Introduction

Thermal power plant has traditionally operated under base-load conditions, where operating steam pressures and temperatures were highly consistent throughout the life of the power plant. However, energy demand is not consistent. More energy is used during the day than at night. Businesses require more energy during weekdays than at weekends. Advances in technology allow for real-time monitoring of energy demand and a more responsive energy network. Next-generation thermal power plant can adjust output to avoid oversupply of energy with associated wasted fuel and added costs. This responsive operating condition is known as load-following operation.

Load-following operation increases plant efficiency but it can lead to early failure of current-generation plant components. Increases and decreases in operating temperatures and pressures lead to fluctuating thermal, mechanical and thermomechanical loadings. This fluctuation exposes plant components to high-temperature fatigue, creep-fatigue and thermomechanical fatigue.

Fatigue loading causes early failure in 9Cr steels (e.g. P91, P92) due to strain-induced microstructure degradation, as shown by Sauzay et al. [1]. Welded components are particularly vulnerable to microstructure degradation due to microstructure changes which occur during the welding process.

9Cr steel parent metal (PM) has good high-temperature strength due to its hierarchical microstructure and precipitate nano-strengthening. Carefully-controlled heat-treatment processes create a PM with optimally-sized prior-austenite grains (PAG), precipitates of optimal size and with optimal spacing and with martensitic laths of optimal widths. Welding subjects this PM microstructure to high temperatures and heating-rates, which compromise the microstructure and thus the high-temperature strength.

The present study considers five main regions in a welded joint, namely the weld metal (WM), the coarse-grained, fine-grained and intercritical heat-affected zones (CGHAZ, FGHAZ, ICHAZ), and the PM. The ICHAZ and FGHAZ are of particular importance as they are traditionally the regions in which failure occurs in welded 9Cr steel components. This failure is known as Type IV failure [2]. Most work on Type IV cracking has focused on creep-dominated failure but high-temperature fatigue also produces ICHAZ failure, according to Farragher et al. [3] and Shankar et al. [4].

This work presents a through-process modelling methodology for simulation of welding and in-service operation of 9Cr steel components. The through-process methodology is implemented in four stages:

- A thermal model simulates the laying of separate weld beads and the heating and cooling experienced by the component.

* Corresponding author: p.macardghail1@nuigalway.ie

- A microstructure evolution model uses the temperature history from the thermal model to predict the evolution of solid-state phases, PAGs, precipitates, laths and hardness.
- A physically-based, temperature-dependent constitutive model uses the temperature history from the thermal model to apply thermal, metallurgical and transformation strains and the microstructure evolution to define the constitutive modelling parameters during welding.
- The 9Cr steel component is subjected to mechanical loading (load-following operation in the current work) and the physically-based constitutive model with its weld-predicted modelling parameters is used to predict mechanical performance.

2 Method

The first part of the through-process model is a purely thermal analysis. The FE geometry is described in Fig. 1. First, the whole FE model is heated to 350°C to represent inter-pass temperatures. All of the weld passes except for the first one are deactivated using Abaqus's 'model change' interaction. The first weld bead is heated using a temperature boundary condition which heats it from 0°C to 1505°C in 1s and holds at 1505°C for 0.5s. The boundary condition is then deactivated and the weld bead is allowed to cool for 45s. The next bead is activated over a period of 0.01s and then its temperature boundary condition is applied and so on until the final weld bead. The final weld bead has a longer cooling time, followed by a cooling boundary condition which reduces the temperature linearly to room temperature. This final cooling is done to expedite the analysis. Heat transfer is controlled by assigning the thermal properties from Yaghi et al. [5].

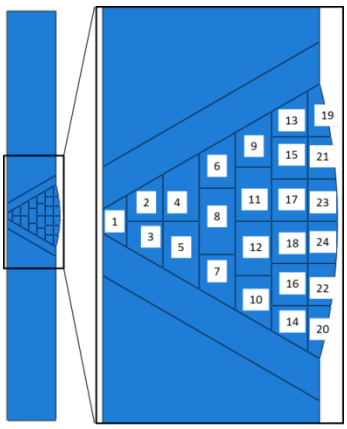

Fig. 1. A schematic of the FE geometry used in the present study with the order of the weld beads highlighted.

The second part of the methodology involves the microstructural model. There are five key microstructure parameters modelled in the present work. The first part involves phase evolution, namely of austenite, delta-ferrite, and untempered martensite. The PM is assumed to exist in a tempered state before welding.

Austenite transformation, a rapid process in this model, is described using a simple lever rule relating austenite volume fraction, V_γ, to temperature:

$$V_\gamma = 1 - \frac{A_{c3} - T}{A_{c3} - A_{c1}} \tag{1}$$

T is the current temperature between A_{c1} (830°C) and A_{c3} (924°C) [6]. The formation of delta ferrite follows a similar equation but with different transformation temperatures A_{c4} (1250°C) and A_{c5} (1450°C), based on the phase-transformation diagram for 9Cr steels [7]. If the grain size is predicted to be small (less than 1 μm) then the delta ferrite will resist transformation back to austenite upon cooling and become retained delta-ferrite in the weld. Austenite can similarly be retained as it cools, otherwise it transforms into martensite, which is considered 'untempered':

$$V_{\alpha'} = \lambda\left(1 - \exp\left[-0.011\left(M_s - T\right)\right]\right) \tag{2}$$

T is the current temperature below M_s (400°C) and λ is a constant used to ensure the volume fraction reaches a value of 1.

When the material transforms to austenite, the grain size evolves. Recrystallisation, represented by the recrystallized volume fraction, S, occurs according to:

$$\Delta S = \lambda_2 \Delta T \tag{3}$$

Due to the rapid nature of recrystallisation during welding, the authors considered a linear relationship using the constant λ_2 to be sufficient for the model. The volume fraction, S, controls grain size during recrystallization:

$$d = \left(d_0 - d_{\min}\right)\left(1 - S\right) + d_{\min} \tag{4}$$

In Eqn. 4, d is the grain size, d_0 is the original grain size, $d_{\min}$ is a minimum grain size (to prevent grains of zero or negative sizes). After the recrystallization is complete, the grains grow as follows:

$$\dot{d} = \left(\lambda_3 - \lambda_4\right)\left(d_{\lim} - d\right) + \lambda_5 \tag{5}$$

In Eqn. 5, $d_{\lim}$ is an asymptotic value of d towards which d rapidly converges. The rate term is divided into and isothermal term, λ_3, and a thermally-transient term, λ_4. During welding, λ_4 dominates and during heat treatment (HT), λ_3 dominates. After d reaches the value of $d_{\lim}$, further growth continues according to λ_5. Eqns. 3, 4 and 5 were calibrated against published heat treatment and simulated welding data from the literature [8, 9].

Material hardness evolves according to:

$$\dot{H} = \lambda_6\left(H_{\lim} - H\right) \tag{6}$$

Eqn. 6 is what will be described in the rest of the paper as an 'asymptotic' equation, including a rate-term, here λ_6, and a limit term, $H_{\lim}$. $H_{\lim}$ can be a large number at

high temperature, e.g. during normalising, which will increase the hardness, H, to produce a hardened, untempered martensite state. At lower, tempering temperatures, H_{lim} may be smaller than H, leading to softening. Eqn. 6 was calibrated against HT data for P91 [10].

The evolution of lath-width is described as follows:

$$\dot{L}_w = \lambda_7\left(L_{w\text{lim}} - L_w\right) - \lambda_8\dot{H} \tag{7}$$

The first term in Eqn. 7 is an asymptotic term to account for rapid lath-coarsening during PWHT or tempering. This part of Eqn. 7 was calibrated against data from [9]. The second term accounts for longer-term lath-coarsening during heat-treatment. This term was calibrated against data from [11].

The precipitate size evolution is described as follows:

$$\dot{m} = \lambda_9\left(m_{\text{lim-1}} - m\right) + \lambda_{10}\left(m_{\text{lim-2}} - m\right) \tag{8}$$

The first asymptotic term in Eqn. 8 is for HT and the second asymptotic term is for ageing and creep. The first asymptotic term was calibrated against data from [9] and the second asymptotic term was calibrated against data from Zielinska et al. [12] and Guguloth et al. [13].

The third part of the through-process methodology, the mechanical model, has three aspects – monotonic stress-strain response, cyclic softening and long-term, creep-type damage. The three aspects are present in the main visco-plastic equation, shown here in uniaxial form:

$$\dot{\varepsilon}_p = \alpha\sinh\left(\beta f\right) \tag{9}$$

where f is the yield function, described as:

$$f = \frac{|\sigma - \chi|}{1 - D - D_c} + R - \sigma_y \tag{10}$$

where D is plasticity-damage, D_c is creep-type-damage, R is isotropic softening and χ is kinematic hardening. The kinematic hardening is based on a Taylor-type, dislocation-based formulation:

$$\dot{\chi} = \frac{\varsigma MGb\dot{\rho}}{\sqrt{\rho}} \tag{11}$$

where M is the Taylor factor, G is the material's shear modulus, b is the magnitude of the Burgers vector and ζ is a multiplicative constant. Dislocation-density evolution occurs according to:

$$\dot{\rho} = \frac{\rho_0\dot{\bar{\rho}}}{\left(1 - \bar{\rho}\right)^2} \tag{12}$$

ρ_0 is the initial dislocation density and $\bar{\rho}$ is a normalised dislocation density, which has a value between 0 and 1, according to:

$$\bar{\rho} = 1 - \frac{\rho_0}{\rho} \tag{13}$$

This definition of normalised dislocation-density was used by Li et al. [14].

Normalised dislocation-density evolves according to:

$$\dot{\bar{\rho}} = c_1\left(\bar{\rho}_{\text{lim}} - \bar{\rho}\right)\left|\dot{\varepsilon}_p\right| \tag{14}$$

$\bar{\rho}_{lim}$ is a temperature-dependent value between 0 and 1, calibrated against 9Cr steel test data and c_1 is a temperature-dependent rate-term.

As similar set of equations is adopted for the cyclic evolution of R, as follows:

$$\Delta R = \frac{\varsigma MGb\Delta\rho_{cyc}}{\sqrt{\rho_{cyc}}} \tag{15}$$

$$\Delta\rho_{cyc} = \frac{\rho_0\Delta\bar{\rho}_{cyc}}{\left(1 - \bar{\rho}_{cyc}\right)^2} \tag{16}$$

$$\bar{\rho}_{cyc} = 1 - \frac{\rho_0}{\rho_{cyc}} \tag{17}$$

ρ_{cyc} is taken as a cyclic dislocation-density, which evolves upon load-reversal. The dislocation-density accumulated during plastic loading (Eqn. 10) is used to update the 'cyclic' dislocation density:

$$\Delta\bar{\rho}_{cyc} = c_{1-cyc}\left(\bar{\rho}_{\text{lim}-cyc} - \bar{\rho}_{cyc}\right)\bar{\rho} \tag{18}$$

This distinction between dislocation density within a cycle and between cycles is described schematically in Fig. 2, showing the change in $\bar{\rho}$ and the definition of $\Delta\bar{\rho}_{cyc}$.

Damage evolution is controlled via a linear relationship with plastic strain:

$$\dot{\omega}_1 = a_1\left|\dot{\varepsilon}_p\right| \qquad \varepsilon_p > a_2 \tag{19}$$

This damage term was calibrated against monotonic data. Equation 19 describes post-necking damage, hence the threshold plastic strain, a_2. A second damage term of a similar form describes final catastrophic damage, as follows:

$$\dot{\omega}_2 = a_3\left|\dot{\varepsilon}_p\right| \qquad \varepsilon_p > a_4 \tag{20}$$

The justification for Eqns. 19 and 20, as well as parameters a_2 and a_4, is displayed schematically in Fig. 3. Combined, the damage term is as follows:

$$\dot{D} = \dot{\omega}_1 + \dot{\omega}_2 \tag{21}$$

Equation 21 corresponds to plasticity damage primarily associated with the manufacturing process, as opposed to in-service operation. For in-service conditions, creep damage is important. Creep test data

from [13], was analysed to approximate creep-type damage, as follows:

$$\dot{D}_c = \frac{a_5 \dot{m}}{L_w} \qquad e_c^{Ideal} > 0.045 \qquad (22)$$

This damage term is microstructure-driven. In this case, precipitate-coarsening $\dot{m}$ is the main driving force, although narrow, untempered laths accelerate the damage evolution. e_c^{Ideal} is a threshold value above which long-term, creep-type damage occurs. This threshold value is derived from creep strain data recorded in [13]. The tertiary creep, assumed to correspond to the onset of damage, appeared to occur at an approximate creep-strain of 0.045 under three different conditions. The present work does not attempt to simulate creep strain, which would require its own constitutive model, e.g. a power-law model, such as in [15], or a hyperbolic sine model, such as in [16]. Instead, the creep-strain data was correlated with microstructure and microstructure-evolution data and is presented here as an idealised creep-strain, as follows:

$$\dot{e}_c^{Ideal} = \frac{c_3 \dot{m}}{L_w} \qquad (23)$$

The identification of Eqns. 22 and 23 is illustrated in Fig. 4, with Eqn. 23 corresponding to Fig. 4b and Eqn. 22 corresponds to Fig. 4c.

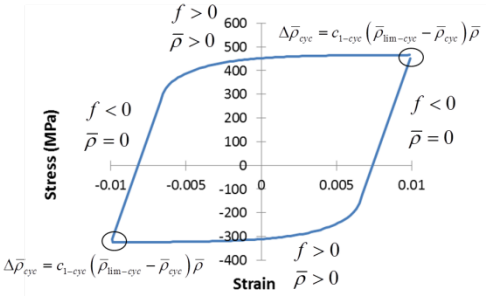

Fig. 2. A schematic representation of the dislocation-density evolution within and between fatigue cycles.

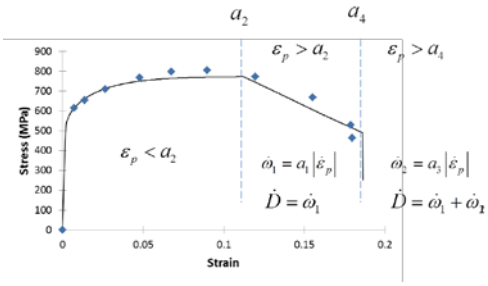

Fig. 3. A schematic representation of the separate plasticity-damage parameters acting on a sample monotonic stress-strain curve (Data points from [6]).

After the FE model is welded, PWHT was applied to the whole geometry (750°C for 70 minutes, as per ISO/TR 14745). The constitutive model was able to predict residual stresses. The residual stresses relaxed during PWHT if the material hardness was reducing due to PWHT (Eqn. 6). In this case, the stress reduced according to a similar asymptotic equation, using the same rate-term as in Eqn. 6 but with an asymptotic value of 0 MPa.

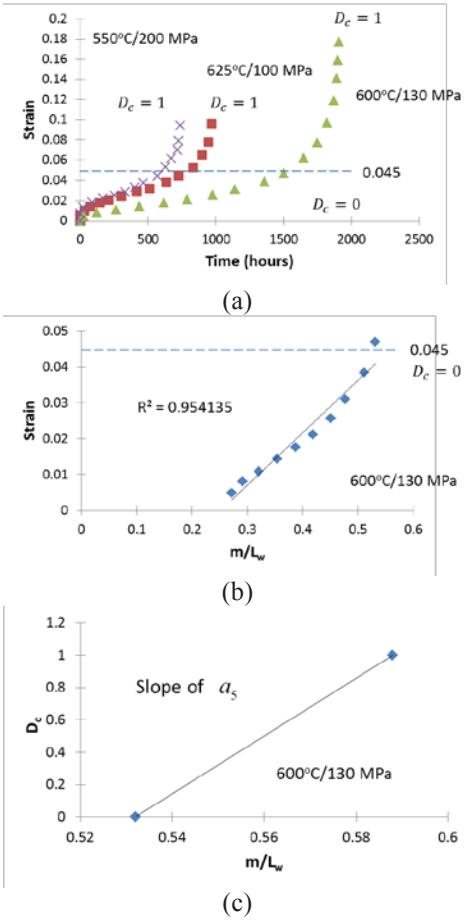

Fig. 4. (a) Creep-test data, from [13], showing the assumptions of threshold creep strain, and initial and final creep-damage values, (b) the correlation between creep-strain, the precipitate diameter, m, and the lath-width, L_w, up to the threshold value for one (sample) set of creep-test data, and (c) the correlation between creep-damage, the precipitate diameter, m, and the lath-width, L_w for one (sample) set of creep-test data.

After PWHT was simulated, an internal pressure load and a temperature boundary condition were applied, based on plant data. Based on the data, the material was cycled between 616°C and 570°C and between 8.5 MPa and 12.5 MPa (see Fig. 5a and 5b), with drops to 80°C and 0 MPa to simulate shutdowns. Each operating cycle, from start-up to shutdown, was modelled as lasting 57 hours.

Several FE elements were sampled along the inside surface of the FE pipe to gather data for microstructure and residual stress in the PM, HAZ and at the weld centreline (WCL). Due to the duration of in-service loading, the authors decided to expedite the simulation by using the sampled data in a uniaxial code.

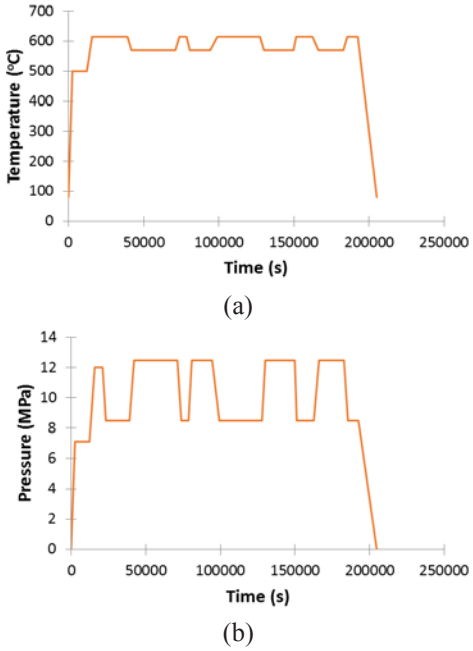

Fig. 5. The proposed cyclic operating conditions for the simulated plant component, (a) temperature and (b) pressure

The internal pressure (Fig. 5b), was converted into an equivalent stress using Lamé's equations for a thick-walled pipe. This equivalent stress was converted to an equivalent strain for the purposes of the material model, which is a strain-controlled. Microstructure equations were retained to enable in-service microstructure changes. The as-welded and PWHT cases for the pipe were both simulated.

Each load cycle is approximately 57 hours long (Fig. 5). It was decided to simulated one year's worth of service (8766 hours, approx 154 cycles) and to compare the results for the different sampled points.

3 Results

3.1. Microstructure evolution - Welding

The results of the microstructure model are as follows. Figure 4 shows the as-welded case. In Fig. 6a, the PM PAG size (38 µm) is unaffected; a thin, fine-grained (9 to 13 µm) region results from the welding, consistent with the FGHAZ, and then the PAG sizes grow until they reach their largest size in the WM (55 µm). In Fig. 6b, the WM is predicted to be a harder region than the PM (447 kgf/mm^2, 226 kgf/mm^2, respectively), although it is clear that the later weld passes softened the earlier passes via auto-tempering, consistent with results found in [6][6]. In Fig. 6c, the predicted precipitate sizes are displayed showing clear evidence of auto-tempering, with precipitates in the earlier weld beads being larger than those in the final weld beads. The as-welded laths in the WM and HAZ are narrower than the unaffected PM, as expected (Fig. 6d).

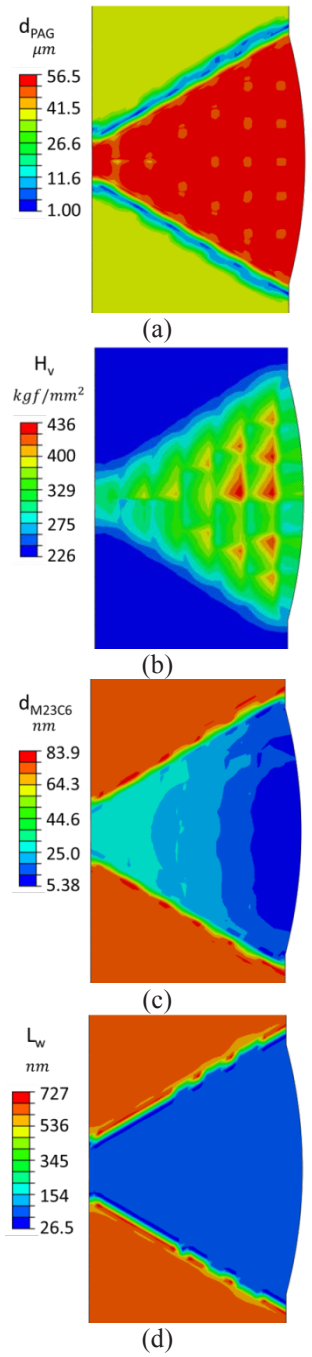

Fig. 6. As-welded microstructure predictions for (a) prior-austenite grains, (b) Vickers hardness, (c) precipitates and (d) lath width.

Following PWHT (Fig. 7), the hardness values equalise across the HAZ, with values ranging from 251 kgf/mm^2 to 208 kgf/mm^2. Laths in the WM grow from 30 nm to 500 nm, while the PM laths grow from 603 mm to 643 mm, though the FGHAZ still sees some relatively narrow laths (380 nm). The precipitates grow from between 8 and 28 nm in the WM to 69 nm, compared to the PM's 76 nm. Thus PWHT is predicted to homogenise the HAZ.

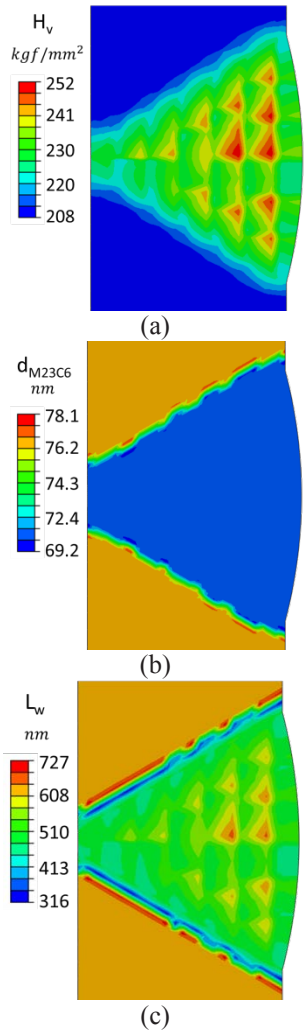

Fig. 7. Microstructure predictions for (a) hardness, (b) precipitates and (c) lath width after PWHT.

3.2. In-service modelling

The sampled points (Fig. 8) for the in-service analysis are described in Tables 1 and 2, for the as-welded and PWHT cases, respectively. Each value is the average value of the four integration points in the sampled element. The stress values correspond to equivalent residual stress.

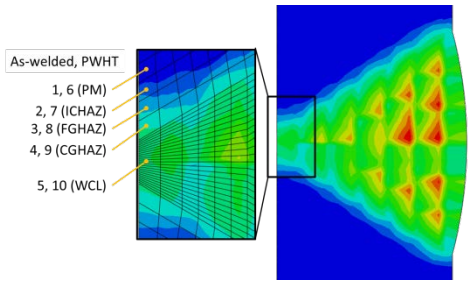

Fig. 8. An illustration of the sampled points (1 to 5 for the as-welded case, 6 to 10 for the PWHT case) extracted from the FE simulation for use in in-service modelling.

The PM was identified by the fact that its microstructure was unaffected by the welding process. The ICHAZ was identified because its slightly reduced PAG size compared to the PM indicated partial recrystallization, and therefore only partial austenite transformation.

Table 1. A description of the sampled points along the pipe wall interior in the as-welded condition

Point	PAG (μm)	Position	Stress (MPa)	Hardness (kgf/mm^2)	Lath width (nm)	Precip. Dia. (nm)
1	38	PM	237	226	603	76
2	27.5	ICHAZ	401	239	575	74
3	9.65	FGHAZ	404	257	189	31.6
4	42.1	CGHAZ	436	273	41	8.46
5	55.2	WCL	473	293	29	8.48

Table 2. A description of the sampled points along the pipe wall interior in the PWHT condition

Point	PAG (μm)	Position	Stress (MPa)	Hardness (kgf/mm^2)	Lath width (nm)	Precip. Dia. (nm)
6	38	PM	43.6	208	643	76.3
7	27.5	ICHAZ	76.7	210.5	638	75
8	9.65	FGHAZ	75.2	214	449	70.3
9	42.1	CGHAZ	79.1	217	443	69.2
10	55.2	WCL	83.1	220	452	69.2

The FGHAZ and CGHAZ both fully transformed to austenite during welding but they could be distinguished by their PAG sizes. The location of the WCL was known from the geometry of the weld rather than by its microstructure.

The predicted time to failure, t_f, in hours, for each of the sample points are displayed in Fig. 9 and Table 3. Table 3 includes the relative increase in life from the as-welded condition, t_f^{AW}, to the PWHT condition, t_f^{PWHT}.

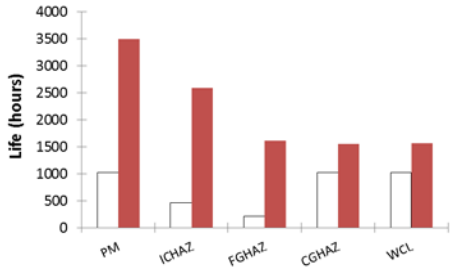

Fig. 9. The predicted time to failure for each of the sample points in the as-welded (empty bars) or PWHT (filled bars) condition.

For the as-welded case, the best predictor of in-service performance was the PAG size, with an R^2 value of 0.83 (see Fig. 10). Relating PAG size to the PWHT case did not provide a useful correlation; however a better correlation was found by using hardness (R^2 =

0.80), the lath-widths (R^2 = 0.87) or the precipitate size (R^2 = 0.93, see Fig. 11).

Table 3. The predicted times to failure for each of the sample points, and the relative increase in life caused by PWHT.

Point	t_f^{AW}	**Point**	t_f^{PWHT}	$\frac{t_f^{PWHT}}{t_f^{AW}}$
1	1026	6	3500	3.4
2	456	7	2590	5.7
3	218	8	1614	7.4
4	1015	9	1553	1.5
5	1018	10	1564	1.5
3	**218**	9	**1553**	**7.1**

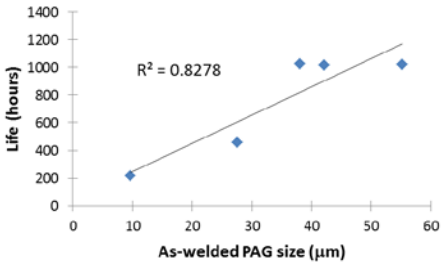

Fig. 10. The correlation between the predicted time to failure for each of the sample points in the as-welded condition and the predicted PAG sizes.

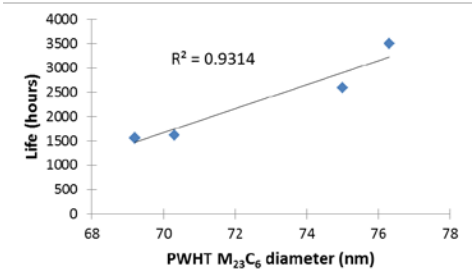

Fig. 11. The correlation between the predicted time to failure for each of the sample points in the PWHT condition and the predicted carbide diameters.

4 Discussion

The thermal model follows a well-established methodology of using block-dumped weld-bead elements to heat the surrounding PM. Heat-transfer properties from previously-published work [5] were adopted. The sequentially-coupled thermal and mechanical analysis is a common way to model welding processes [17, 18], and the use of an axi-symmetric model is a common way of modelling pipe components, which has been shown to give reasonable results compared to 3D models [19, 20].

The microstructure evolution model is based on test data from the literature. This gives the authors confidence that it can accurately represent microstructure evolution; however the model has a large number of modelling parameters which could be reduced via the use of even more physically-based models, e.g. the lath-width evolution model in [21].

The constitutive model is based on a range of conventional modelling approaches, e.g. Taylor hardening, Kocks-Mecking dislocation-density evolution, hyperbolic sine functions, etc. Relating constitutive modelling parameters to microstructure features is typical of physically-based modelling.

The in-service aspect of the model was applied uniaxially to sample points rather than to the entire FE geometry (Fig. 6). Ideally, the load-following conditions would be applied to the FE geometry but the authors found this to be too computationally-expensive and time-consuming for the current work. A full FE in-service simulation will be attempted in future work.

The as-welded pipe is predicted to have significantly lower service life than the PWHT pipe. This is an expected and encouraging result. There were some interesting predictions made as to the relative performance of different weld regions. The location with the lowest life in the PWHT pipe is predicted to be the CGHAZ, contrary to expectations regarding Type IV cracking, although there is little difference between predicted IC-FGHAZ, CGHAZ and WM lives. This indicates that the PWHT successfully removed any regions which were obviously weak compared to other regions.

Failure was dominated by the long-term damage term (Eqn. 22) compared to plasticity damage (Eqn. 21). For the most part, yield did not occur in the material under the prescribed loading conditions and when it did, the plastic strain was insufficient to activate plasticity damage.

The weakest point in the as-welded pipe was the FGHAZ, as expected [2, 22]. PWHT extended the life of this region by a factor of 7.4. The as-welded CGHAZ and WM both had similar predicted lives, as expected from their similar microstructures (Table 1).

The as-welded CGHAZ and WM might seem as though they should predict the shortest lives but their high hardness allows for in-service tempering and relaxation of residual stresses. The in-service tempering allowed the lath-width to increase, thus slowing the onset of long-term damage (Eqns. 22, 23). The FGHAZ is not sufficiently hard for tempering to occur and its detrimental microstructure takes its toll on the predicted in-service life.

PWHT appears to have been most beneficial for the PM and ICHAZ regions by conferring them with the widest laths. This indicates that damage and failure are

less likely to occur in these regions. This is somewhat contrary to expectations concerning the ICHAZ; however, ICHAZ failure occurs in fine-grained ICHAZ regions [22], whereas the ICHAZ region predicted by this work has coarser grains.

The predicted in-service lives correlated well with PAG size in the as-welded case, mainly because it was possible for the other microstructure features to evolve during service. For the PWHT samples, however, the microstructures were more-or-less in their final form and less likely to be affected by in-service loading, so all microstructure features except PAG sizes could serve as indicators of performance.

Quantitatively, the model predicts very short lives for all sampled regions. The longest predicted life was just 3500 hours, or 146 days, or 0.4 years. This is most likely due to the idealisations and assumptions introduced in Eqns. 22 and 23. Future work will require a more detailed and rigorous creep-type damage model but, for the present study, Eqns. 22 and 23 provide the through-process methodology with some capability to predict in-service performance. The qualitative trends predicted by this work are promising. Overall, this work presents a step towards a through-process model for power plant steels and a step towards a weld design tool for industry.

5 Conclusions

- Multi-pass welding and PWHT was simulated for a thick-walled, 9Cr steel, pipe component.
- Microstructure evolution, including grain size evolution, distribution of tempered and untempered regions, hardness, martensitic laths and precipitate size, was modelled.
- Auto-tempering effects were captured in the model and PWHT was predicted to equalise the HAZ microstructure.
- The welding simulation predicted a fine-grained region a short distance from the fusion zone, consistent with the IC-FGHAZ. PWHT does not fully recover the microstructure of this region, leaving relatively narrow laths.
- Realistic load-following plant operating conditions were simulated for discrete points sampled from the pipe interior to represent the PM, ICHAZ, FGHAZ, CGHAZ and WM in both the as-welded and PWHT conditions.
- The as-welded pipe was predicted to have a significantly shorter service life than the PWHT pipe, with the fine-grained region being the first to fail. The PWHT pipe predicted a similar life for the FGHAZ, CGHAZ and WM and that failure initiates between the FGHAZ and the WM.

6 Acknowledgements

This research is funded by Science Foundation Ireland grant number SFI/14/IA/2604. The authors would like to acknowledge the contributors to this research; NUI Galway, the Ryan Institute, General Electric (UK), ESB International, University of Limerick, Imperial College, London and Fraunhofer IWM, Freiburg. The authors would also like to thank Mr. S. Scully for supplying load-following plant temperature and pressure data for use in this work.

7 References

1. M. Sauzay, H. Brillet, I. Monnet, M. Mottot, F. Barcelo, B. Fournier, A. Pineau, Mat. Sci. Eng. A **400-401** (2005)
2. J. A. Francis, W. Mazur, H. K. D. H. Bhadeshia, Mat. Sci. Tech. **22**, 12 (2006)
3. T. P. Farragher, S. Scully, N. P. O'Dowd, C. J. Hyde, S. B. Leen, J. P. V. T. **136** (2014)
4. V. Shankar, R. Sandhya, M. D. Mathew, Mat. Sci. Eng. A, **528** (2011)
5. A. H. Yaghi, T. H. Hyde, A. A. Becker, J. A. Williams, W. Sun, J. Mat. Proc. Tech. **167** (2005)
6. A. H. Yaghi, T. H. Hyde, A. A. Becker, W. Sun, J. P. V. P. **111-112** (2013)
7. H. Cerjak, Proc. International Conference Safety and Reliability of Welded Components (2008)
8. L. Milovic, T. Vuherer, I. Blacic, M. Vrhovac, M. Stankovic, Materials and Design **46** (2013)
9. P. J. Ennis, A. Czyrska-Filemonowicz, O. M.M. I. **1** (2002)
10. G. Potirniche, I. Charit, K. Rink, F. Barlow, NEUP 2009 Project, **09-835** (2013)
11. D. R. Barbadikar, G. S. Deshmukh, L. Maddi, K. Laha, P. Parameswaran, A. R. Ballal, D. R. Peshwe, R. K. Paretkar, M. Nandagopal, M. D. Mathew, I. J. P. V. P. **132-133** (2015)
12. A. Zielinski, M. Miczka, B. Boryczko, M. Sroka, Archives of Civil and Mechanical Engineering, **16** (2016)
13. K. Guguloth, J. Swaminathan, N. Roy, R. N. Ghosh, Mat. Sci. Eng. A, **684** (2017)
14. H. Li, J. Lin, T. A. Dean, S. W. Wen, A. C. Bannister,. I. J. Plasticity, **25** (2009)
15. S. Khayatzadeh, D. W. J. Tanner, C. E. Truman, P. E. J. Flewitt, Eng. Frac. Mech., **175** (2017)
16. C. Ó Murchú, S. B. Leen, P. O'Donoghue, R. A. Barrett, Mat. Sci. Eng. A, **682** (2017)
17. K. Abburi Venkata, C. E. Truman, R. C. Wimpory, T. Pirling, I. J. P. V. P. (2017) (In press)
18. L. E. Lindgren, Computer methods in applied mechanics and engineering, **195** (2006)
19. P. Dong, J. P. V. T. **123** (2001)
20. D. Deng, H. Murakawa, Comp. Mat. Sci., **37** (2006)
21. E. I. Galindo-Nava, P. E. J. Rivera-Diáz-del-Catillo, Acta Materialia, **98** (2015)
22. J. S. Lee, K. Maruyama, Metallurgical Materials International, **21** (2015)